High-resolution geophysical monitoring of moisture accumulation preceding slope movement – a path to improved early warning

A. Watlet[1,2], P. Wilkinson[1], J. Whiteley[3,1], A. White[1], S. Uhlemann[4,1], R. Swift[1], S. Ouellet[5], C. Minto[6], P. Meldrum[1], L. Jones[1], D. Gunn[1], A. Godfrey[6], B. Dashwood[1], R. Crickmore[7], P. Clarkson[6], J. Boyd[1], J. Chambers[1]

[1]British Geological Survey, Nottingham, UK

[2]Geology and Applied Geology, University of Mons, Belgium

[3]AtkinsRéalis, Bristol, UK

[4]Lawrence Berkeley National Laboratory, Berkeley, USA

[5]University of Calgary, Canada

[6]Indeximate, Hinckley, Leicestershire, LE10 1AQA

[7]Luna OptaSense

Corresponding author: Arnaud Watlet (arnw@bgs.ac.uk)

Peer-review status:

This is a non peer-reviewed preprint (v1), submitted to *EarthArXiv*. The manuscript has been submitted for consideration in *Environmental Research Letters*.

Abstract

Slope failures are an ongoing global threat leading to significant numbers of fatalities and infrastructure damage. Landslide impact on communities can be reduced using efficient early warning systems to plan mitigation measures and protect elements at risk. This manuscript presents an innovative geophysical approach to monitoring landslide dynamics, which combines Electrical Resistivity Tomography (ERT) and low-frequency Distributed Acoustic Sensing (DAS), and was deployed on a slope representative of many landslides in clay rich lowland slopes. ERT is used to create detailed, dynamic moisture maps that highlight zones of moisture accumulation leading to slope instability. The link between ERT derived soil moisture and the subsequent initiation of slope deformation is confirmed by low-frequency DAS measurements, which were collocated with the ERT measurements and provide changes in strain at unprecedented spatiotemporal resolution. Auxiliary hydrological and slope displacement data support the geophysical interpretation. By revealing critical zones prone to failure, this combined ERT and DAS monitoring approach sheds new light on landslide mechanisms. This study demonstrates the advantage of including subsurface geophysical monitoring techniques to improve landslide early warning approaches, and highlights the importance of relying on observations from different sources to build effective landslide risk management strategies.

1 Introduction

Slope failures are a threat to communities around the globe. They cause significant damage to critical infrastructure and individual properties and in some cases may lead to loss of life. In recent history, landslides led to >4500 recorded fatalities per year (Froude & Petley, 2018), and billions of dollars of economic losses (Dilley, 2005; Kirschbaum et al., 2015). Even non-fatal, minor landslides may have large economic impacts as they affect critical infrastructure (Emberson et al., 2020). These numbers are set to increase due to climate change and associated global rise in rainfall intensity, which is a major trigger of landslides (Gariano & Guzzetti, 2016). While preventing landslides from occurring is impractical due to costs, the associated risks can be mitigated both at local and regional scales to reduce landslide impacts on society (Lacasse et al., 2009). A better understanding of the morphology of unstable slopes, and the associated slope failure mechanisms is key to developing more informed risk management strategies. Monitoring of unstable slopes, in particular, is an essential component of local landslide Early Warning Systems (Lo-LEWS) (Maskrey, 2011), which main purpose is to identify precursors of landslide events (Intrieri et al., 2013) and locate zones that may become unstable due to changes in the subsurface conditions.

Moisture-induced landslides are those triggered by increased soil moisture or groundwater levels, which raise pore water pressures and hence reduces effective stresses. Basic Lo-LEWS monitoring approaches mainly integrate surface displacement observations, indicating ongoing deformation but not detecting the underlying cause. Therefore, Lo-LEWS can benefit from monitoring subsurface parameters related to the driving factors of slope failure to extend the effective warning period (Lacroix et al. 2020). Geophysics-based monitoring systems have emerged as powerful tools to track subsurface conditions of slopes prone to moisture-induced landslides (Whiteley et al., 2019), increasing the predictive capacity of slope failure (Uhlemann et al., 2021). Designed to non-invasively image the subsurface, and providing proxies to critical slope stability properties (e.g. moisture, suction, shear strength), geophysical methods are ideally equipped to assess the integrity of unstable slopes at various scales (Whiteley et al., 2021) .

Electrical Resistivity Tomography (ERT) has long been used to investigate landslides in 2D or 3D (Jongmans & Garambois, 2007), providing electrical resistivity models linked to the geology, hydrology and morphology of the landslide. More recently, time-lapse ERT (i.e. in 4D) has increasingly been applied to monitor landslides (Bièvre et al., 2012; Gance et al., 2016; Hojat et al., 2019; Lapenna & Perrone, 2022; Lehmann et al., 2013; Perrone et al., 2014; Supper, 2014; Tsai et al., 2021; Watlet et al., 2023; Whiteley et al., 2023). The main benefits of geoelectrical monitoring lie in the possibility to link changes in electrical resistivity to changes in subsurface conditions, mainly moisture (Holmes et al., 2022; Slater & Binley, 2021), coupled with the maturity of remote monitoring equipment specifically designed for autonomous monitoring of slope processes (Chambers *et al.* 2022). At the other end of the near-surface geophysics spectrum, Distributed Acoustic Sensing (DAS) systems have rapidly emerged as novel tools capable of detecting seismic signals (Dou et al., 2017). More recently, DAS has shown great potential in the low-frequency domain (<1Hz) to monitor dynamic changes in strain (Crickmore et al., 2020; Karrenbach et al., 2019).

We present, to the best of our knowledge, the first 4D ERT imaging of slope movement supported by strain measurements from low-frequency DAS, and hydrological and geotechnical datasets. With this study, we aim to demonstrate the advanced capability to detect precursory conditions to slope displacement. Incorporating 4D soil moisture data in the feed of information used to assess slope stability has the potential to improve landslide early warning strategies, thereby enhancing landslide risk mitigation.

2 Site description and methodology

2.1 The Hollin Hill Landslide Observatory (HHLO)

The HHLO (Fig. 1, Chambers et al. 2011; Gunn et al. 2013) in North Yorkshire, UK, was designed in the mid-2000s as a test site for developing novel geophysical monitoring of unstable slopes. The site features a moisture-induced, slow-moving landslide, representative of many clay-rich lowland landslides worldwide. It has a well-documented history of seasonal reactivation with peaks in movement generally occurring during winter, between December and March (see Fig. S1 in the Supplementary material). The landslide's morphology largely depends on the underlying geological structure. The south-facing slope comprises two main geological units (Lower to Late Jurassic) gently dipping to the North: the Whitby Mudstone Formation (WMF) and the Staithes Sandstone Formation (SSF). Due to lower permeability and high plasticity, the WMF slowly creeps over the SSF when reaching elevated moisture contents. This translational movement mostly occurs in the central part of the slope. In the top part, a complex rotational failure within the WMF is observed, linked to the mass wasting generated by creeping downslope (Uhlemann et al. 2017; Boyd et al. 2021). The hydrogeological context of the HHLO includes the occurrence of perched water tables at shallow depth (Gunn *et al.* 2013) overlying a deeper regional groundwater table.

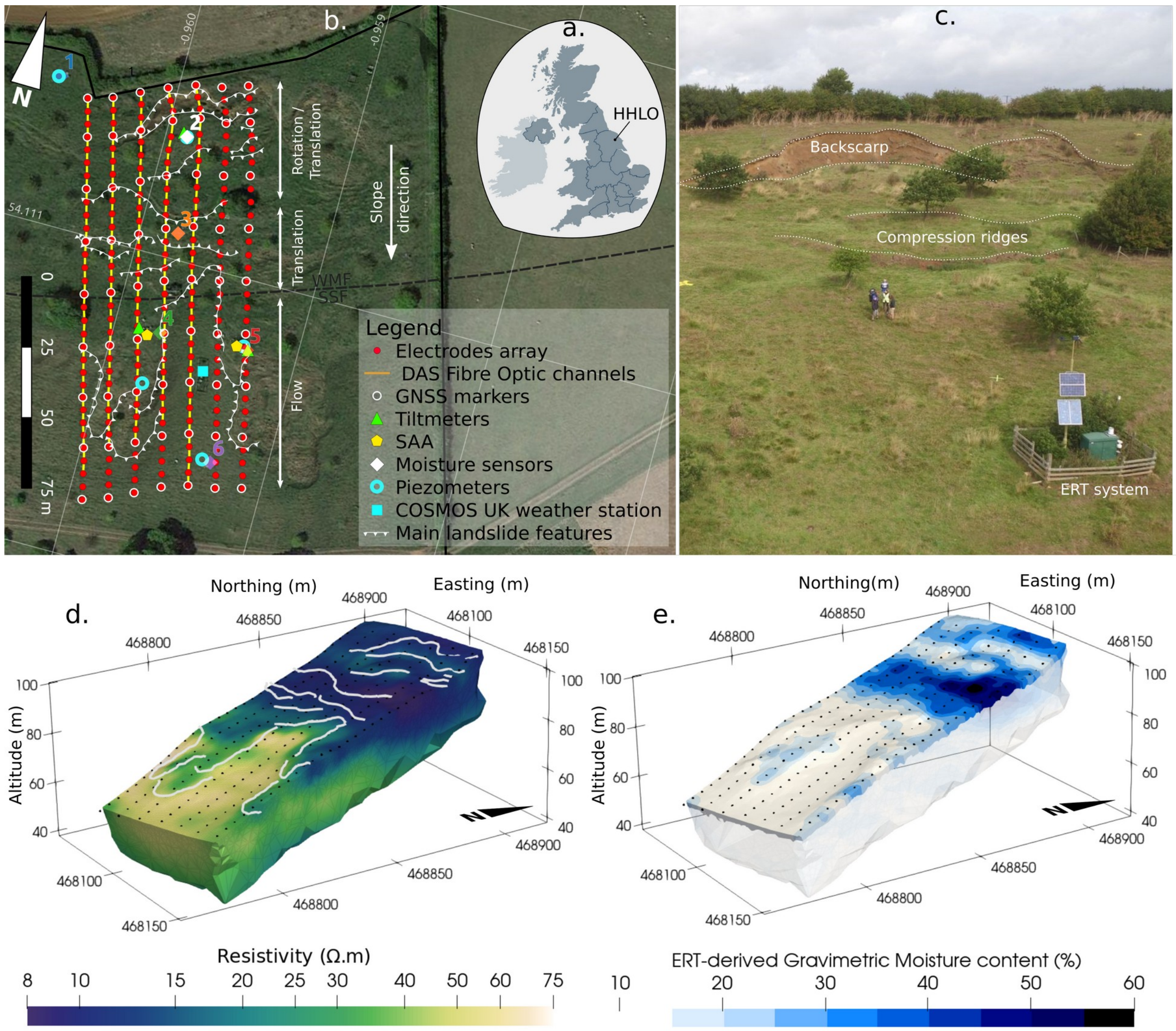

Figure 1: a) Location of Hollin Hill on UK map, b) Map of the HHLO displaying the location of the ERT array, fibre optic cable, point sensors (and location number), GNSS markers and main landslide features; c) Drone photo highlighting the backscarp and compression ridges of the HHLO. d) Resistivity model and e) ERT-derived GMC model for the monitoring baseline (22 November 2020).

Since first deployed in 2008, 4D geoelectrical imaging revealed complex, seasonal moisture dynamics in the slope (Uhlemann et al. 2017; Merritt et al. 2018). Preferential infiltration and moisture build-up have also been linked with periods of increased movements, and evidence of superficial drying processes are associated with surface shrinking and cracking. However, properly demonstrating that local zones of elevated moisture content were leading to co-located displacement or slope failure has been challenging. One main reason has been the challenge of monitoring slope deformation at a spatial and temporal scale comparable to that of time-lapse ERT measurements (Kelevitz et al. 2021). Deriving electrode movements from time-lapse ERT measurements was successfully developed (Wilkinson et al. 2015, 2016), providing a means of tracking large displacements greater than 10% of the electrode spacing. But other techniques providing independent measurement of surface deformation at higher resolution, such as strain from low-frequency DAS, ideally complement the toolbox of monitoring techniques able to detect minor movements precursory to larger slope failure.

Over the years, state-of-the-art sensors have also been deployed at the HHLO to provide independent measurements for comparison and interpretation alongside geophysics-based monitoring. Clusters of point sensors including shallow soil moisture (at 20 cm and 50 cm bgl), matric potential (at 50 cm bgl) and piezometers monitoring water level in shallow and deep boreholes are distributed over 6 locations (1-6 in Fig. 1). Ground deformation associated with the landslide activity is also tracked via four independent approaches at the HHLO, including tiltmeters (at location 2, 4 and 5), Shape Accelerometers Arrays (SAA; Abdoun *et al.* 2013) (at location 4 and 5), GNSS marker pegs and repeated LiDAR scans (see Table S1 and Text S3 in the Supplementary material for more details; Lague et al., 2013)

2.2 Gravimetric Water Content from Electrical Resistivity Tomography

The PRIME system installed since November 2020 at the HHLO is a low-cost and low-power ERT instrument designed for remotely monitoring slope condition (Holmes et al. 2020). ERT measurements are acquired on a scheduled, daily basis and telemetered to remote servers through 4G internet. The ERT array comprises seven lines oriented in the slope direction, each with 32 electrodes, forming a grid of 224 electrodes with a separation of 9.5 m across the slope and 4.75 m along the slope (see Fig. 1). A comparable ERT array layout was installed for a decade (2008 – 2019) at the HHLO (Kuras et al. 2009), and proved to capture shallow hydrological processes throughout the hillslope (Uhlemann *et al.* 2017; Merritt *et al.* 2018). ERT time-lapse inversion follows a hybrid inversion scheme mimicking a time-lapse inversion but incorporating potential electrode movements as monitored by repeated GNSS surveys of a network of ground control points (Uhlemann *et al.* 2016; Boyd *et al.* 2021). Since only one large slope displacement event occurred within the time window presented in this manuscript (22 November 2020 to 30 March 2022), electrode locations have been adapted only once following this event. Adjusted electrode locations are derived from inverting the ERT data for electrode movements, following a methodology developed in (Wilkinson *et al.* 2015, 2016).

In this study, we present ERT monitoring results as soil moisture models. Resistivity models are translated into Gravimetric Moisture Content (GMC) models after inversion and temperature correction, following the approach by Uhlemann et al. (2017), calibrated for the HHLO by Merritt et al. (2016) using Waxman & Smits (1968) relationships (Fig 1. d-e). The calibration was performed on soil and shallow borehole core samples from the SSF and WMF. We use separate parameter sets for the WMF and the SSF as in Uhlemann et al. (2017). Boyd et al. (2024) has highlighted that this relationship is likely to be valid only at shallow depths, given that Waxman-Smits equation parameters change for deeper, more consolidated rocks. Therefore, the GMC models are generated using the relationship developed by Uhlemann et al. (2017) applied to the first 2 m below the ground surface, which represents the layer above mapped shear zones. However, due to the presence of perched water levels at ~2m below ground level (bgl), especially in the WMF, most temporal changes in resistivity, and therefore GMC, are expected to occur at shallow depth. More detailed on the acquisition and processing of the ERT data is available in Text S1 (Brunet et al., 2010; Keller & Frischknecht, 1966; Mwakanyamale et al., 2012)

2.3 Strain from low-frequency Distributed Acoustic Sensing

We rely on strain measurements acquired by a DAS system along a fibre optic cable deployed at the HHLO (Clarkson *et al.* 2021). The DAS system consists of a Luna Optasense ODH-F interrogator unit which transmits coherent laser pulses within the fibre, and acts as a distributed interferometer. Any strain disturbance to the fibre changes the optical phase of the backscattered light (Bao & Chen, 2012; Bao & Wang, 2021) and can be recorded. A low-pass filter at 1 Hz is applied to the DAS data and optical phase data are converted to units of strain. The fibre was buried at ~10 cm bgl within narrow trenches along the slope direction to form six lines, five of which are co-located with the easternmost five lines of the ERT array. The strain measurements derived from low-frequency DAS are sampled with a 1 m spatial interval over a gauge length of 4 m, which defines the spatial resolution (detailed processing in Text S2 of the Supplementary material). In this study, we investigate change in strain averaged at daily time intervals on two periods overlapping the ERT dataset from 22 November 2020 to 30 January 2021 (70 days), and then from 22 November 2021 to 28 February 2022 (100 days), each focusing on the wettest part of the season. Data are expressed as cumulative change in microstrain (με) with respect to a baseline set at the beginning of each period.

3 Results and discussion

3.1 Moisture accumulation preceding landslide reactivation

The ERT-derived soil moisture dataset of this study starts on 22 November 2020. Increase in GMC is displayed at regular intervals before the main slope displacement event on 20-21 January 2021 (Fig. 2). This increase is most pronounced in the WMF formation, especially above the backscarp and in the area of the rotational slip, with localised increases higher than 10% GMC. This general moisture trend is corroborated by the network of soil moisture sensors. The backscarp itself stays relatively dry, contrasting with the zone directly above and below. The steepness of the scarp combined with locally lower permeability near the slip plane favors surface run-off processes, hindering in-situ water infiltration. The resistivity models in the backscarp region also show preferential flow between the zone above the scarp and the flatter region at the toe of the scarp, favoring moisture accumulation (see Fig S2 in the Supplementary material).

Deformation data show that the 2021 reactivation started with two minor precursory displacement events (in the order of 1 mm recorded by the shallowest SAA at 10 cm bgl) following rainfall events, on 27 December 2020 and 14 January 2021 (Fig. 3). The first precursor event seems to have predominantly affected the middle part of the slope, where change in microstrain indicates compression in the mid-slope ridges (Fig. 4). The second precursory event followed snowfall and is documented using strain data from the low-frequency DAS at 1 minute sampling frequency in Ouellet et al. (2024). It started with mid-slope deformation, then propagated upslope to the backscarp. The main deformation occurred on 20-21 January 2021, as Storm Christophe hit the UK. Deformation was mainly confined to the top part of the slope underneath the backscarp, as corroborated by the microstrain data (Fig. 3c), with two main transverse zones of compressions on existing ridges, and extension in the backscarp. The top-slope tiltmeter recorded a tilt step of 0.3° in the slope direction, indicating rotational processes. The mid-slope tiltmeters showed no change, although the western SAA recorded ~12 mm horizontal displacement, indicating minor translational movement mid-slope (Fig. 3b). Following this main event, two minor events were visible in the tiltmeters and SAA data on 29 January

2021 and 19 February 2021, with respectively 2 mm and 1 mm as recorded by the SAA, as well as 0.04° and 0.02° recorded by the top-slope tiltmeter.

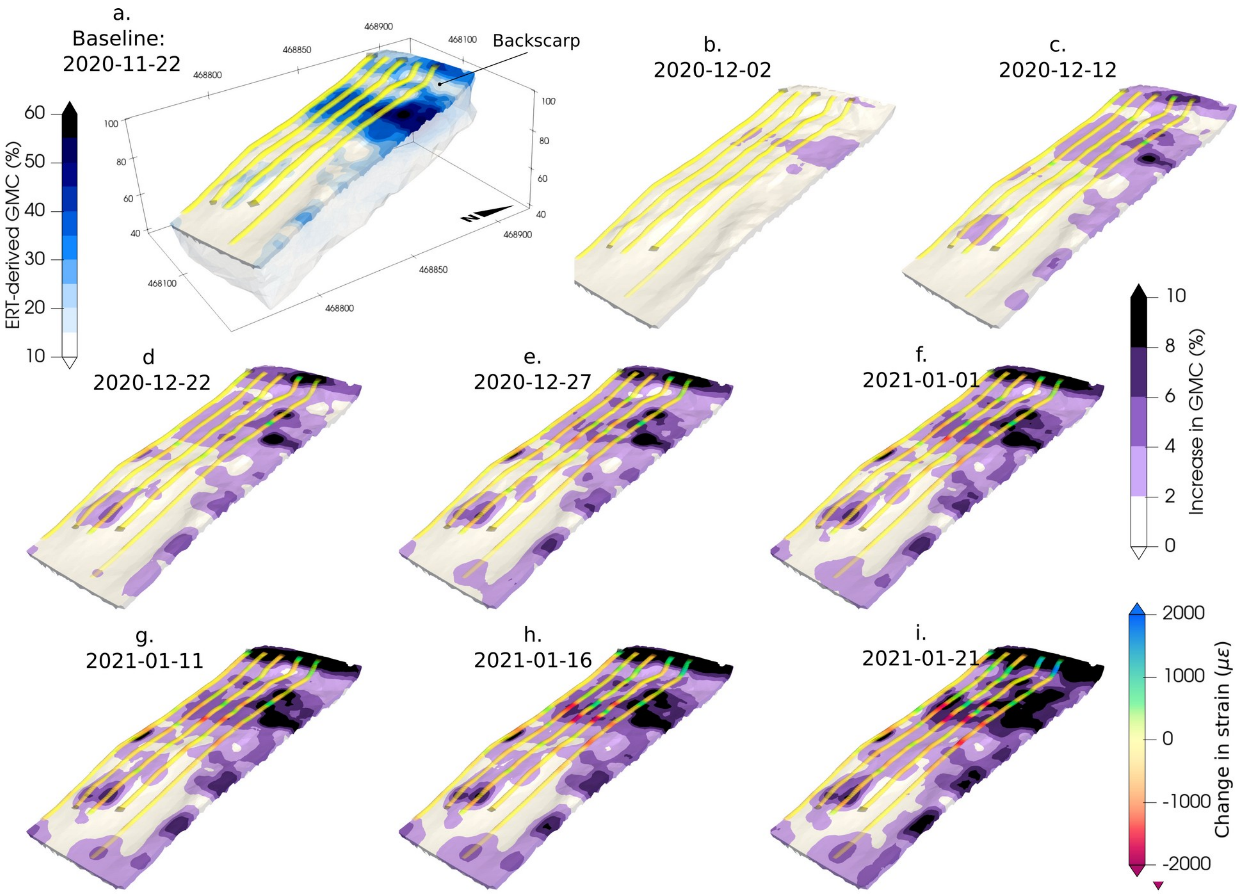

Figure 2: ERT-derived Gravimetric Moisture Content (GMC) model for the baseline on 22 November 2020 (a), and models of relative increase in GMC with respect to the baseline displayed on a selection of time-steps (b-i). Recorded changes in microstrain are also shown.

In 2022, the landslide remained comparatively stable, with only a few minor deformation events. Each observed deformation in 2022 is visible in only one of the datasets from DAS (Fig. 3i), SAA, or the top-slope tilt-meter (Fig. 3h), indicating much smaller and more localized deformation than in 2021. This is confirmed by the GNSS surveys and LIDAR scans which detected no noticeable surface topography variation.

3.2 Landslide mechanism

A joint analysis of vertical displacement (from LIDAR surveys), horizontal displacement (from GNSS markers), tilt data and downslope strain (from low-frequency DAS) during the 20-21 January event highlights rotational movement mainly in a small area underneath the backscarp, where ground elevation increased below a zone of extension on the fiber. This area coincides with the GNSS marker with the highest horizontal displacement, confirming a combination of translational and rotational movement, limited to the top half of the slope. Despite a lack of temporal resolution in the geophysics-based data, comparing tilt change at the top of the slope and displacement data from the central slope SAA suggests similar dynamics as described by Ouellet et al. (2024), with central slope destabilization and horizontal displacement propagating and amplifying upslope, including a rotational component when reaching the backscarp zone. During the 14 January precursory event, high temporal resolution low-frequency DAS (Ouellet et al. 2024) showed that this retrogressional behavior propagated from the central slope to the backscarp at ~1.7 m/h. Similar retrogressive dynamics were also identified at larger timescales by large mobilization of the flow lobes in 2013 followed by the development of the backscarp in 2016.

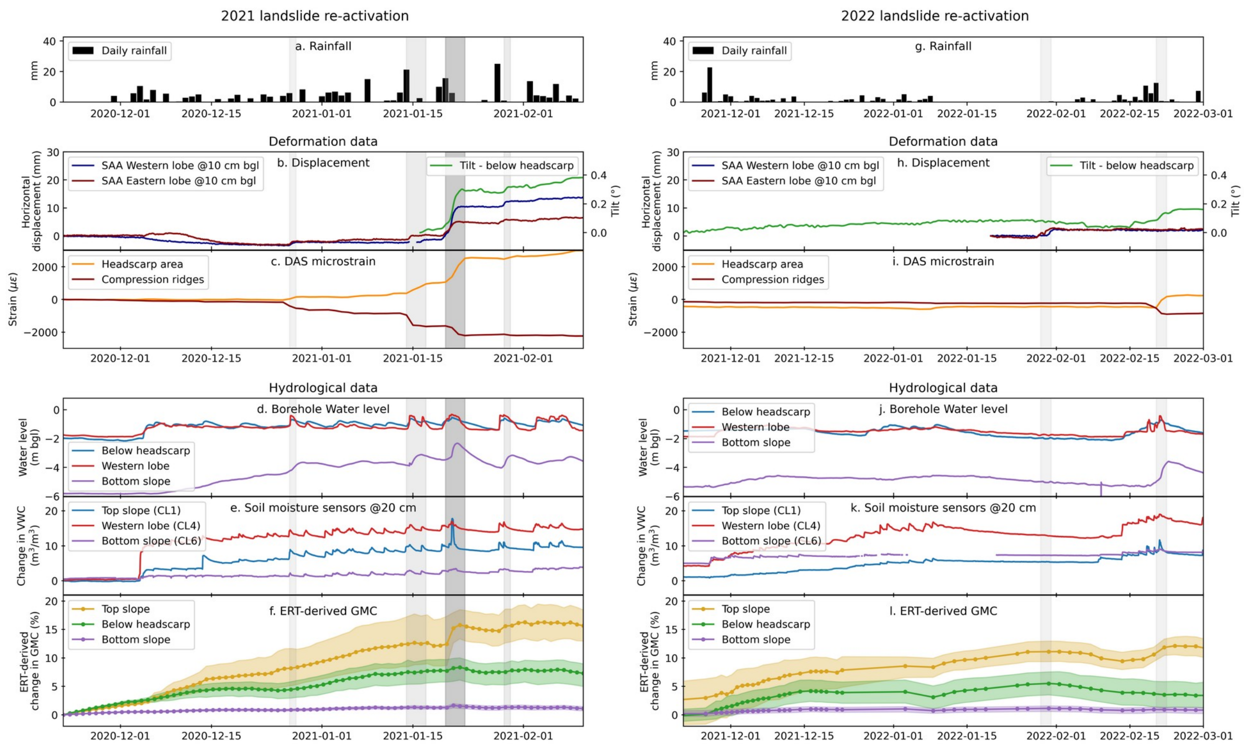

Figure 3: Summary of the geophysical, hydrological and displacement datasets acquired during the 2021 (a-f) and 2022 (g-l) landslide reactivation periods (November 2020 to February 2021, and November 2021 to March 2022). Figures display rainfall (a, g), surface displacement (b, h), DAS microstrain (c, i) using channels highlighted in Fig. S3, borehole water level (d, j), soil moisture at 20 cm bgl (e, k), ERT-derived GMC (f, l). Grey boxes indicate periods of minor (light grey) and major (dark grey) deformation event.

The top-slope tiltmeter showed significant downslope tilt starting on 20 January 2021 around 20:00 UTC, peaking between 02:00 and 03.00 UTC on 21 January 2021, coinciding with a peak in moisture content at the top of the slope. Peak displacement lasted 15 hours, as inferred from the tilt data. This event cannot be related to a particularly extreme rainfall event, with only 10 and 15.6 mm on 19 and 20 January. Rainfall on 20 January was low but sustained, becoming more intense towards the evening with 9.59 mm recorded over 4 hours starting from 20:00, peaking at 22:00. Despite the daily rainfall being unremarkable, this 4-hour event was the most intense since summer 2020 and the second highest over winter 2021, linked to smaller movements recorded by the SAA and tiltmeters.

However, the main deformation event and precursors occurred in the area with the highest moisture content (>40% GMC and up to 55% GMC) as established by the ERT monitoring, and the highest increase in moisture with respect to the baseline (> 10% GMC, Fig. 2). This confirms elevated soil moisture as the driving factor for ground displacement, with

WMF mudstone material potentially reaching a local liquid limit. GMC higher than 55% matches with liquid limits previously measured on WMF soil samples (Merritt et al. 2014) and fits well with previously obtained thresholds for landslide activation of 49% (Uhlemann et al., 2017). Data from moisture sensors and piezometers show high peaks in moisture and water level starting at 22:00, which are hard to explain solely by local rainfall. As a consequence of Storm Christophe hitting the UK, heavy rain with spatially varying intensity was recorded in Northern England (Met Office, 2021). It is likely that the event was triggered by surface or subsurface run-off from that plateau upslope, temporarily saturating parts of the hillslope already at high moisture levels. Rain rate data from NIMROD MET-Office rainfall radar (over 1 km² cells and 5 min intervals; (Met Office, 2003)) reveals that more intense rainfall occurred just north of the site, on the plateau directly upslope of the hill.

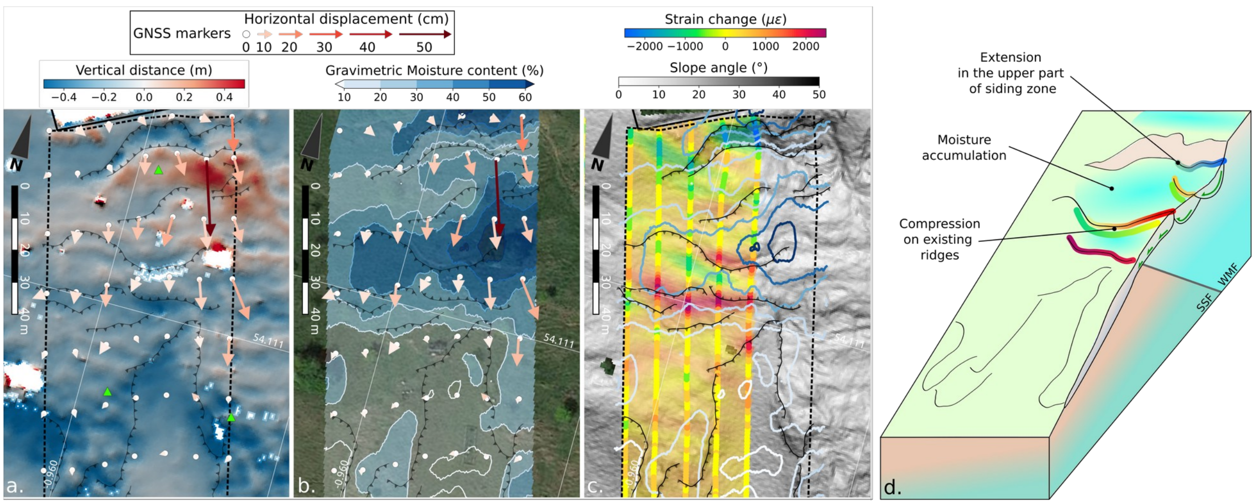

Figure 4: Maps showing a) vertical displacement computed from LiDAR scans from November 2020 and September 2021, and horizontal displacement on the network of GNSS markers between 15 January 2021 and 20 February 2021; b) ERT-derived GMC following peak movement in landslide reactivation 2021 (22 January 2021) as compared to GNSS markers displacement; c) Strain change recorded on the fibre and interpolated, and compared to GMC contour lines following peak movement (22 January 2021) ; d) Sketch describing the landside dynamics at the HHLO and the geophysical observations on the ERT and DAS monitoring systems.

3.3 Combining ERT and low-frequency DAS and implications for landslide early warning

This study highlights the complementarity of ERT and low-frequency DAS to reveal the mechanisms leading to slope deformation with unprecedented detail. The ERT-based moisture imaging provides time-lapse snapshots of the subsurface with high spatial resolution, setting the moisture condition context throughout the slope. Despite the 3D ERT-based GMC models being displayed on a relatively fine mesh, the overall resolution depends on the electrode separation, which is relatively sparse at the HHLO (see Sect. 2). This layout has the benefit of sampling a large portion of the hillslope, while limiting the capability of the system to image subtle shallow resistivity changes but providing spatially continuous images at depths closer to the expected slip surface. This is precisely where the complementarity with the low-frequency DAS is most powerful. By providing strain data at shallow depth (~10 cm), with high spatial resolution along the FO cable, i.e. in the slope direction, it provides direct and localised information on slope stability in the near surface where the ERT system has poor sensitivity.

The ERT-derived moisture models accurately delineate zones of interest (Fig. 4d) where moisture slowly builds up, and the WMF clay materials are above the plastic limit, locally reaching the liquid limit. Slope deformation occurred in an area that showed elevated moisture contents in the weeks prior to movement. The low-frequency DAS complements these observations by identifying strain changes at the edge of the zones of elevated moisture, as minor displacement occurs. This demonstrates that calibrated time-lapse ERT providing spatio-temporal soil moisture dynamics, effectively validates elevated soil moisture as the cause of slope movement, and identifies zones where landslide susceptibility increases. DAS strain data then sheds light on how the elevated moisture translates in terms of slope stability. Crucially, the co-location of these measurements allows time-lapse imaging of holistic slope processes that cannot be practicably replicated using point sensors nor rainfall data alone. This makes it extremely valuable for both sources of geophysical information to jointly feed a new generation of Lo-LEWS looking at changes in co-related material properties (Bogaard and Greco 2018; Segoni et al. 2018; Whiteley et al. 2021), with a particular interest in the surveillance of critical infrastructures, such as long linear assets (e.g. railway cutting, flood embankment, etc.).

Datasets acquired at the HHLO prior to the relatively minor slope deformation event in 2021 also help to improve the definition of thresholds that can be used to issue Lo-LEWS alarms for future, potentially larger events. For instance, no significant movement was recorded in 2022. Comparing the ERT-derived moisture models from January 2021 and during winter 2022 shows that moisture was at lower levels throughout the slope, particularly in the top of the slope where zones with the highest moisture contents remained below the thresholds of the January 2021 event (Figs. 3f, 3l).

4 Summary

This study presents the deployment of a long-term ERT and strain monitoring from low frequency DAS at the Hollin Hill Landslide Observatory (HHLO), together with a network of hydrological and geotechnical sensors and techniques. It represents, to the best of our knowledge, the first combination of ERT and DAS monitoring on an active slow-moving landslide. Through a robust and already well documented methodology, daily 3D electrical resistivity models are transformed into shallow soil moisture models at high spatial resolution. These reveals zones of moisture accumulation in the top part of the slope, which eventually led to slope movement, with a peak in January 2021, as revealed with an unprecedented spatial resolution by changes in strain measured by the low-frequency DAS along a fibre optic cable co-located with the ERT array.

Results from this interdisciplinary approach highlight the efficacy of integrating multiple geophysical methods together to enhance the observability and understanding of landslide mechanisms. A notable strength of this approach lies in the capability of ERT, via high-spatial resolution imaging, to delineate zones of elevated moisture content, which can be interpreted as precursory indicators of slope instability. Unlike point sensors, which do not provide spatially continuous measurements of subsurface properties, the ERT and DAS monitoring capability described in this study can provide high-resolution spatiotemporal images that allow a holistic assessment of subsurface processes at the whole-slope scale. This study offers novel ways to address the critical need to advance the observational capability in slope stability analysis, which will inevitably lead to improved early warning systems and to better informed risk management strategies, and therefore enhance the resilience of societies to landslide hazards worldwide.

Acknowledgments

BGS authors publish with the permission of the Executive Director, British Geological Survey (UKRI-NERC). We would like to thank Josie Gibson, Frances Standen and James Standen for their continued support at Hollin Hill. We also thank Brendon Purnell from Luna Optasense, and members of Environmental & Engineering Geophysics at BGS, including Mihai Cimpoiasu, Harry Harrison, Jessica Holmes, Cornelia Inauen, Oliver Kuras and Dave Morgan for their help and support. Processed data from ERT, low-frequency DAS, soil moisture sensors, tilt-meters, Shape Accelerometer Arrrays, LiDAR scans, GNSS surveys are available at Zenodo via https://doi.org/10.5281/zenodo.13118623 with Creative Commons Attribution 4.0 International license (British Geological Survey, 2024). ERT data were pre-processed using Pandas (McKinney et al., 2010), and Resipy (Blanchy et al, 2020; https://resipy.org), inversions were performed using E4D (Johnson et al., 2010; https://www.pnnl.gov/projects/e4d). Figures were created using Matplotlib (Hunter et al., 2007); Paraview (Ahrens et al., 2005), Qgis and InkScape.

References

Abdoun, T., Bennett, V., Desrosiers, T., Simm, J. & Barendse, M., 2013. Asset Management and Safety Assessment of Levees and Earthen Dams Through Comprehensive Real-Time Field Monitoring. *Geotech Geol Eng*, **31**, 833–843. doi:10.1007/s10706-012-9569

Ahrens, J., Geveci, B., Law, C., Hansen, C., & Johnson, C. (2005). Paraview: An end-user tool for large-data visualization. *The visualization handbook*, *717*, 50038-1.

Bao, X., & Chen, L. (2012). Recent progress in distributed fiber optic sensors. *Sensors*, *12*(7), pp.8601-8639.

Bao, X., & Wang, Y. (2021). Recent Advancements in Rayleigh Scattering-Based Distributed Fiber Sensors. *Advanced Devices & Instrumentation*, *2021*, 2021/8696571. https://doi.org/10.34133/2021/8696571

Bièvre, G., Jongmans, D., Winiarski, T., & Zumbo, V. (2012). Application of geophysical measurements for assessing the role of fissures in water infiltration within a clay landslide (Trièves area, French Alps). *Hydrological Processes*, *26*(14), 2128-2142.

Blanchy, G., Saneiyan, S., Boyd, J., McLachlan, P. and Binley, A., 2020. ResIPy, an intuitive open source software for complex geoelectrical inversion/modeling. *Computers & Geosciences*, *137*, p.104423.

Boyd, J., Chambers, J., Wilkinson, P., Peppa, M., Watlet, A., Kirkham, M., Jones, L., *et al.*, (2021). A linked geomorphological and geophysical modelling methodology applied to an active landslide. *Landslides*, 1–16, Springer.

Boyd, J. P., Binley, A., Wilkinson, P., Holmes, J., Bruce, E., & Chambers, J. (2024). Practical considerations for using petrophysics and geoelectrical methods on clay rich landslides. *Engineering Geology*, *334*, 107506.

British Geological Survey. (2024). Data used in manuscript "High-resolution geophysical monitoring of moisture accumulation preceding slope movement – a path to improved early warning". https://doi.org/10.5281/zenodo.1311862

Brunet, P., Clément, R., & Bouvier, C. (2010). Monitoring soil water content and deficit using Electrical Resistivity Tomography (ERT) – A case study in the Cevennes area, France. *Journal of Hydrology*, *380*(1–2), 146–153. https://doi.org/10.1016/j.jhydrol.2009.10.032

Chambers, J.E., Wilkinson, P.B., Kuras, O., Ford, J.R., Gunn, D.A., Meldrum, P.I., Pennington, C.V.L., *et al.*, (2011). Three-dimensional geophysical anatomy of an active landslide in Lias Group mudrocks, Cleveland Basin, UK. *Geomorphology*, **125**, 472–484. doi:10.1016/j.geomorph.2010.09.017

Chambers, J., Holmes, J., Whiteley, J., Boyd, J., Meldrum, P., Wilkinson, P., Kuras, O., Swift, R., Harrison, H., Glendinning, S., Stirling, R., Huntley, D., Slater, N. & Donohue, S. (2022). Long-term geoelectrical monitoring of landslides in natural and engineered slopes. *The Leading Edge*, 41, 768-776.10.1190/tle41110768.1

Clarkson, P., Crickmore, R., Godfrey, A., Minto, C., Purnell, B., Gunn, D., Dashwood, B., *et al.*, (2021). Ground Condition Monitoring of a Landslide using Distributed Rayleigh Sensing. *EAGE GeoTech 2021 Second EAGE Workshop on Distributed Fibre Optic Sensing*, Vol. 2021, pp. 1–5, European Association of Geoscientists & Engineers.

Crickmore, R., Godfrey, A. & Minto, C., (2020). Temperature and Strain Separation from a Distributed Rayleigh System. *EAGE Workshop on Fiber Optic Sensing for Energy Applications in Asia Pacific*, Vol. 2020, pp. 1–4, European Association of Geoscientists & Engineers.

Dilley, M. (2005). *Natural disaster hotspots: a global risk analysis* (Vol. 5). World Bank Publications.

Dou, S., Lindsey, N., Wagner, A.M., Daley, T.M., Freifeld, B., Robertson, M., Peterson, J., *et al.*, (2017). Distributed acoustic sensing for seismic monitoring of the near surface: A traffic-noise interferometry case study. *Scientific reports*, **7**, 1–12, Nature Publishing Group.

Emberson, R., Kirschbaum, D. & Stanley, T., (2020). New global characterization of landslide exposure. *Natural Hazards and Earth System Sciences Discussions*, **2020**, 1–21, Göttingen, Germany.

Froude, M.J. & Petley, D.N., (2018). Global fatal landslide occurrence from 2004 to 2016. *Natural Hazards and Earth System Sciences*, **18**, 2161–2181, Copernicus GmbH.

Gance, J., Malet, J.-P., Supper, R., Sailhac, P., Ottowitz, D. & Jochum, B., (2016). Permanent electrical resistivity measurements for monitoring water circulation in clayey landslides. *Journal of Applied Geophysics*, **126**, 98–115. doi:10.1016/j.jappgeo.2016.01.011

Gariano, S.L. & Guzzetti, F., (2016). Landslides in a changing climate. *Earth-Science Reviews*, **162**, 227–252, Elsevier.

Gunn, D.A., Chambers, J.E., Hobbs, P.R.N., Ford, J.R., Wilkinson, P.B., Jenkins, G.O. & Merritt, A., (2013). Rapid observations to guide the design of systems for long-term monitoring of a complex landslide in the Upper Lias clays of North Yorkshire, UK. *Quarterly Journal of Engineering Geology and Hydrogeology*, **46**, 323–336, GeoScienceWorld.

Hojat, A., Arosio, D., Ivanov, V.I., Longoni, L., Papini, M., Scaioni, M., Tresoldi, G. and Zanzi, L., (2019). Geoelectrical characterization and monitoring of slopes on a rainfall-triggered landslide simulator. *Journal of Applied Geophysics*, *170*, p.103844.

Holmes, J., Chambers, J., Meldrum, P., Wilkinson, P., Boyd, J., Williamson, P., Huntley, D., *et al.*, (2020). Four-dimensional electrical resistivity tomography for continuous, near-real-time monitoring of a landslide affecting transport infrastructure in British Columbia, Canada. *Near Surface Geophysics*, Wiley Online Library.

Holmes, J., Chambers, J., Wilkinson, P., Meldrum, P., Cimpoiaşu, M., Boyd, J., Huntley, D., *et al.*, (2022). Application of petrophysical relationships to electrical resistivity models for assessing the stability of a landslide in British Columbia, Canada. *Engineering Geology*, 106613, Elsevier.

Hunter, J. D. (2007). Matplotlib: A 2D graphics environment. *Computing in science & engineering*, *9*(03), 90-95.

Intrieri, E., Gigli, G., Casagli, N. & Nadim, F., (2013). Brief communication" Landslide Early Warning System: toolbox and general concepts". *Natural hazards and earth system sciences*, **13**, 85–90, Copernicus GmbH.

Johnson, T.C., Versteeg, R.J., Ward, A., Day-Lewis, F.D. & Revil, A., (2010). Improved hydrogeophysical characterization and monitoring through high performance electrical geophysical modeling and inversion. *Geophysics*, **75**, WA27–WA41.

Jongmans, D. & Garambois, S., (2007). Geophysical investigation of landslides: a review. *Bulletin de la Société géologique de France*, **178**, 101–112.

Karrenbach, M., Cole, S., Ridge, A., Boone, K., Kahn, D., Rich, J., Silver, K., *et al.*, (2019). Fiber-optic distributed acoustic sensing of microseismicity, strain and temperature during hydraulic fracturing. *Geophysics*, **84**, D11–D23, Society of Exploration Geophysicists.

Keller, G. V., & Frischknecht, F. C. (1966). Electrical methods in geophysical prospecting

Kirschbaum, D., Stanley, T. & Zhou, Y., 2015. Spatial and temporal analysis of a global landslide catalog. *Geomorphology*, **249**, 4–15, Elsevier.

Kuras, O., Pritchard, J.D., Meldrum, P.I., Chambers, J.E., Wilkinson, P.B., Ogilvy, R.D. & Wealthall, G.P., (2009). Monitoring hydraulic processes with automated time-lapse electrical resistivity tomography (ALERT). *Comptes Rendus Geoscience*, **341**, 868–885.

Lacasse, S., Nadim, F., Lacasse, S. & Nadim, F., (2009). Landslide Risk Assessment and Mitigation Strategy. in *Landslides – Disaster Risk Reduction*, pp. 31–61, eds. Sassa, K. & Canuti, P., Springer Berlin Heidelberg. Doi:10.1007/978-3-540-69970-5_3

Lacroix, P., Handwerger, A. L., & Bièvre, G. (2020). Life and death of slow-moving landslides. *Nature Reviews Earth & Environment*, *1*(8), 404-419.

Lague, D., Brodu, N. & Leroux, J., (2013). Accurate 3D comparison of complex topography with terrestrial laser scanner: Application to the Rangitikei canyon (N-Z). *ISPRS Journal of Photogrammetry and Remote Sensing*, **82**, 10–26. doi:10.1016/j.isprsjprs.2013.04.009

Lapenna, V. & Perrone, A., (2022). Time-lapse electrical resistivity tomography (TL-ERT) for landslide monitoring: Recent advances and future directions. *Applied Sciences*, **12**, 1425, MDPI.

Lehmann, P., Gambazzi, F., Suski, B., Baron, L., Askarinejad, A., Springman, S.M., Holliger, K., *et al.*, (2013). Evolution of soil wetting patterns preceding a hydrologically induced landslide inferred from electrical resistivity survey and point measurements of volumetric water content and pore water pressure. *Water Resources Research*, **49**, 7992–8004, Wiley Online Library.

Maskrey, A., (2011). Revisiting community-based disaster risk management. *Environmental Hazards*, **10**, 42–52, Taylor & Francis.

McKinney, W., van der Walt, S., & Millman, J. (2010). Proceedings of the 9th Python in Science Conference.

Merritt, A.J., Chambers, J.E., Murphy, W., Wilkinson, P.B., West, L.J., Gunn, D.A., Meldrum, P.I., *et al.*, (2014). 3D ground model development for an active landslide in Lias mudrocks using geophysical, remote sensing and geotechnical methods. *Landslides*, **11**, 537–550. doi:10.1007/s10346-013-0409-1

Merritt, A.J., Chambers, J.E., Murphy, W., Wilkinson, P.B., West, L.J., Uhlemann, S., Meldrum, P.I., *et al.*, (2018). Landslide activation behaviour illuminated by electrical resistance monitoring: Landslide Activation Behaviour. *Earth Surface Processes and Landforms*, **43**, 1321–1334. doi:10.1002/esp.4316

Merritt, A.J., Chambers, J.E., Wilkinson, P.B., West, L.J., Murphy, W., Gunn, D. & Uhlemann, S., (2016). Measurement and modelling of moisture—electrical resistivity relationship of fine-grained unsaturated soils and electrical anisotropy. *Journal of Applied Geophysics*, **124**, 155–165. doi:10.1016/j.jappgeo.2015.11.005

Met Office, (2003). 1 km Resolution UK Composite Rainfall Data from the Met Office Nimrod System. NCAS British Atmospheric Data Centre. Retrieved from https://catalogue.ceda.ac.uk/uuid/27dd6ffba67f667a18c62de5c3456350

Met Office, (2021). Daily Weather Summary 2021. Retrieved from https://digital.nmla.metoffice.gov.uk/IO_e9deeb04-8105-4f31-94d6-7d94c00b3c21/

Mwakanyamale, K., Slater, L., Binley, A., & Ntarlagiannis, D. (2012). Lithologic imaging using complex conductivity: Lessons learned from the Hanford 300 Area. *Geophysics*, *77*(6), E397–E409.

Ouellet, S.M., Dettmer, J., Lato, M.J., Cole, S., Hutchinson, D.J., Karrenbach, M., Dashwood, B., Chambers, J.E. and Crickmore, R., 2024. Previously hidden landslide processes revealed using distributed acoustic sensing with nanostrain-rate sensitivity. *Nature Communications*, *15*(1), p.6239.

Perrone, A., Piscitelli, S. & Lapenna, V., 2017. Electrical resistivity tomographies for landslide monitoring: a review. *Berichte Geol*, **93**, 129–134.

Slater, L. & Binley, A., (2021). Advancing hydrological process understanding from long-term resistivity monitoring systems. *Wiley Interdisciplinary Reviews: Water*, **8**, e1513, Wiley Online Library.

Supper, R., Ottowitz, D., Jochum, B., Kim, J.H., Römer, A., Baron, I., Pfeiler, S., Lovisolo, M., Gruber, S. and Vecchiotti, F., (2014). Geoelectrical monitoring: an innovative method to supplement landslide surveillance and early warning. *Near Surface Geophysics*, *12*(1), pp.133-150.

Tsai, W.-N., Chen, C.-C., Chiang, C.-W., Chen, P.-Y., Kuo, C.-Y., Wang, K.-L., Lin, M.-L., *et al.*, (2021). Electrical resistivity tomography (ERT) monitoring for landslides: Case study in the lantai area, yilan taiping mountain, northeast taiwan. *Frontiers in Earth Science*, **9**, 737271, Frontiers Media SA.

Uhlemann, S., Smith, A., Chambers, J., Dixon, N., Dijkstra, T., Haslam, E., Meldrum, P., *et al.*, (2016). Assessment of ground-based monitoring techniques applied to landslide investigations. *Geomorphology*, **253**, 438–451. doi:10.1016/j.geomorph.2015.10.027

Uhlemann, S., Chambers, J., Meldrum, P., McClure, P., & Dafflon, B. (2021). Geophysical monitoring of landslides–a step closer towards predictive understanding?. *Understanding and Reducing Landslide Disaster Risk: Volume 3 Monitoring and Early Warning 5th*, 85-91.

Uhlemann, Sebastian, Chambers, J., Wilkinson, P., Maurer, H., Merritt, A., Meldrum, P., Kuras, O., *et al.*, (2017). Four-dimensional imaging of moisture dynamics during landslide reactivation. *Journal of Geophysical Research: Earth Surface*, **122**, 398–418. doi:10.1002/2016JF003983

Watlet, A., Thirugnanam, H., Singh, B., Kumar M., N., Brahmanandan, D., Inauen, C., Swift, R., *et al.*, (2023). 4D electrical resistivity to monitor unstable slopes in mountainous tropical regions: an example from Munnar, India. *Landslides*, **20**, 1031–1044. doi:10.1007/s10346-023-02029-3

Waxman, M.H. & Smits, L.J.M., (1968). Electrical conductivities in oil-bearing shaly sands. *Society of Petroleum Engineers Journal*, **8**, 107–122.

Whiteley, J. S., Chambers, J. E., Uhlemann, S., Wilkinson, P. B. & Kendall, J. M. (2019). Geophysical Monitoring of Moisture-Induced Landslides: A Review. *Reviews of Geophysics*, 57, 106-145.10.1029/2018rg000603

Whiteley, J. S., Watlet, A., Kendall, J. M. & Chambers, J. E. (2021). Brief communication: The role of geophysical imaging in local landslide early warning systems. *Nat. Hazards Earth Syst. Sci.*, 21, 3863-3871.10.5194/nhess-21-3863-2021

Whiteley, Jim, Inauen, C., Wilkinson, P., Meldrum, P., Swift, R., Kuras, O. & Chambers, J., (2023). Assessing the risk of slope failure to highway infrastructure using automated time-lapse electrical resistivity tomography monitoring. *Transportation Geotechnics*, **43**, 101129, Elsevier.

Wilkinson, P., Chambers, J., Uhlemann, S., Meldrum, P., Smith, A., Dixon, N. & Loke, M.H., (2016). Reconstruction of landslide movements by inversion of 4-D electrical resistivity tomography monitoring data: LANDSLIDE MOVEMENTS FROM ERT INVERSION. *Geophysical Research Letters*, **43**, 1166–1174. doi:10.1002/2015GL067494

Wilkinson, P.B., Uhlemann, S., Chambers, J.E., Meldrum, P.I. & Loke, M.H., (2015). Development and testing of displacement inversion to track electrode movements on 3-D electrical resistivity tomography monitoring grids. *Geophysical Journal International*, **200**, 1566–1581. doi:10.1093/gji/ggu483

Supplementary Materials

Text S1. ERT data processing

Data acquisition comprises dipole-dipole measurements with dipole lengths *a* = 1-4 electrode spacings and dipole separations *na* with *n* = 1-7, including full sets of reciprocal readings. ERT data quality assessment includes filtering based on low retrieved voltage, repeatability error and reciprocal error. For each time-steps, apparent resistivities are filtered for outliers above 10% reciprocal error. An error model that weights each transfer resistance in the inversion is constructed for each time steps. We rely on a reciprocal error model employing a multi-bin methodology, which follows the approach outlined by Mwakanyamale et al. (2012). The reciprocal error is defined as the standard error in the mean of the forward and reverse measurements.

Additionally, following a strategy employed in Boyd et al. (2021) a constant factor of 1% of the transfer resistance is added to all reciprocal errors, in order to represent for forward modelling errors. This strategy improves the convergence of the inversion while ensuring the development of spatially and temporally smooth models.

The 3D time-lapse inversion is conducted with the fully parallelised inversion code E4D, as detailed in Johnson et al. (2010). To generate a 3D mesh for the inversion, input data includes surface topography derived from a LiDAR scan calibrated with GNSS control points.

This time-lapse inversion is undertaken on a set of daily time-steps from 22 November 2020 to 30 March 2022. The time-lapse inversion uses smoothness constraints both spatially and temporally. The initial model is computed using a 3D smoothness-constrained inversion of the baseline data. We opt for a L2 norm. Subsequently, each time step is inverted with reference to the baseline. In the time-lapse inversion, we apply an L2 temporal smoothness constraint. A target misfit metric (χ^2) value of 1.0 is assigned to the E4D inversion.

For the time-lapse inversion, it is essential that the dataset of each time step includes identical readings as in the baseline. Readings which are in the baseline sequence but become rejected in subsequent time steps are retained in the inversion but their associated errors are set to the measurement value itself. This results in minimal weight assigned to the rejected data. Generally, a reduced number of measurements in the baseline sequence decreases the overall model sensitivity.

Variations in subsurface temperature can have significant impacts on the electrical resistivity (Brunet et al., 2010). In order to isolate changes in electrical resistivity that can be mainly attributed to changes in soil moisture, one needs to correct the resistivity models for the effects of temperature. We rely on temperature data from a vertical profile of six temperature sensors deployed at depths of 0.1, 0.2, 0.5, 1.0, 2.5, and 4.5 m bgl. in the centre of the ERT array. Given the relatively large electrode separation at the HHLO, the inverted resistivity time-series are poorly correlated with the shallowest three temperature sensors, indicating that shallow changes in temperature don't affect significantly the ERT data. Therefore only data from the deepest three temperature sensors are taken into account in the temperature correction. First, daily 1D temperature profiles are generated by linear interpolation of the temperature data. The 1D temperature profiles are then used to convert the resistivity ρ_T of each cell of the models into standard resistivity ρ_{corr} (at T_{corr} = 20°C) using the linear model of Keller and Frischknecht (1966), valid between 0 and 25°C, which is defined as:

$$\rho_{corr} = \rho_T \left(1 + m(T - Tcorr)\right) \quad \text{(Eq.1)}$$

with a correction factor m = 0.02 °C^{-1} (Uhlemann et al. 2017).

Converting the resistivity models into gravimetric moisture content relies on the methodology described for the HHLO in Uhlemann et al. (2017). This uses a petrophysical relationship relying on the Waxman-Smits model (Waxman & Smits, 1968) for which the parameters were calibrated on soil samples for the two main geological units (SSF and WMF) by Merrit et al. (2016). The two zones are delineated from the baseline resistivity model based on a 28 Ωm threshold in dry conditions, which provides a reasonable estimate of the limit (Boyd et al., 2021).

Text S2. Low-Frequency DAS data processing

The DAS system consists of an interrogator unit housing a laser source that generates coherent laser pulses that are sent along an optical fibre. The fibre acts as a distributed interferometer, where the phase of backscattered light from different sites along the fibre varies as the refractive index and therefore optical path length at those points changes. The refractive index depends on both the strain and temperature of the fibre and therefore a measurement of the phase change of the backscattered light between successive pulses can be used to determine changes in strain and temperature (Bao & Chen, 2012; Bao & Wang, 2021).

The interrogator unit and datalogger are housed in a barn at approximately 700 m from the Hollin Hill slope. The fibre optic cable is linked to the interrogator unit via a tight buffered cable. On the slope, the fibre optic cable was installed along the ERT lines. Practically speaking, in order to keep good coupling of the fibre with surrounding soil materials, the fibre trenches were dug ~5 cm parallel to the trench hosting the ERT cables.

DAS measurements are sampled along the fibre with a 1 m spatial interval over a gauge length of 4 m, which defines the spatial resolution. A low-pass filter at 1 Hz is applied on the raw data, which were acquired at 500 Hz, and optical phase data are converted to units of strain following a methodology described in Ouellet et al. (2024). Since changes in temperature also affect the optical phase, temperature effects are separated using two cables having more sensitive to temperature and running parallel to one of the lines different sensitivities to strain and temperature (Crickmore et al., 2020). The first cable has a "tight-buffered" construction and the fibre is well coupled to both strain and temperature. The second has a "loose-tube" construction and has a much lower strain response. The measured phase changes in each cable for temperature change T and strain change S, are given by the following two equations:

$$P_1 = \alpha_1 T + \beta_1 S \quad \text{(Eq. 2)}$$

$$P_2 = \alpha_2 T + \beta_2 S \quad \text{(Eq. 3)}$$

Where $P1$ and $P2$ are the measured phase changes in cables 1 and 2, respectively; α_1 and α_2 are the temperature sensitivity coefficients of cables 1 and 2, respectively; $\beta 1$ and $\beta 2$ are the strain sensitivity coefficients of cables 1 and 2, respectively. The equations can be solved to give temperature and strain change in terms of the phases $P1$ and $P2$.

A 1-day moving average is then applied to provide daily strain data corrected for temperature. The strain dataset comprises two subsets acquired from 22 November 2020 to 30 January 2021 (70 days), and then from 22 November 2021 to 28 February 2022 (100 days). Daily strain changes are thus calculated from the first day of each of these periods used as baseline, by subtracting strain measurements from subsequent days to the strain average at the baseline. Strain data is expressed in microstrain (με) and provide information on the surface displacements and landslide dynamics (Ouellet *et al.* 2024). Indication of displacement can be inferred from strain by multiplying the microstrain by the gauge length. Although the larger the displacement, the higher the risks of losing coupling between the fibre and the soil, resulting in underestimating actual displacement, as discussed in Ouellet et al. (2024). This has certainly been the case after the major landslide movement of 20-21 January 2021, after which a section of the fibre on Line 5 near the backscarp got exposed, accommodating strain where the slope surface makes a convex angle. Remediation took place in the following weeks to re-bury the exposed section, taking advantage of some slack left at the top of the line.

Text S3. Auxiliary datasets

Clusters of point sensors including shallow soil moisture (at 20 cm and 50 cm bgl), matric potential (at 50 cm bgl) and piezometers monitoring water level in shallow and deep boreholes are distributed over 6 locations (1-6 in Fig. 1). The way the piezometers have been installed (i.e. relatively narrow screened interval) allows the measured water level to be related to the pore pressure. Not all locations feature the same number of sensors, but overall they provide detailed information on the hydrological subsurface conditions within the different landslide domains. A weather station, which is part of the COSMOS-UK network, is installed in the bottom part of the slope and provides, amongst others, rainfall and air temperature data. Additional 1 km² rainfall estimates from the Nimrod MetOffice network of C-band rainfall radars (Met Office, 2003) are also utilised to investigate the spatial variation of rain intensity in the area surrounding the HHLO. Geotechnical sensors comprising three tiltmeters (Geosense Nodes) have been deployed and cover the different landslide domains (at location 2, 4 and 5) and Shape Accelerometers Arrays (SAA, Abdoun *et al.* 2013), located mid-slope on the translational zone of the landslide (at location 4 and 5).

The 56 GNSS markers are manually surveyed with a Leica GS15 system on a regular basis (7 surveys over the 16 months of monitoring featured in this study). The GNSS markers mainly provide accurate horizontal displacement data (±1 cm accuracy), given a lower accuracy in the Z direction (+- 10 cm). They are also used to interpolate the electrode positions as the land surface changes with the landslide movement.

The four LiDAR scans were acquired on the 12 November 2020, 23 March 2021, 27 September 2021 and 15 March 2022 with a Leica Pegasus system. Resulting LiDAR 3D point clouds are used to generate Digital Elevation Models (DEM), and vertical distances between each instance of the point clouds are computed using the M3C2 algorithm (Lague et al., 2013) of the CloudCompare software, thereby providing accurate vertical displacement data (+- 5 cm accuracy) at high spatial resolution. Here we use downsampled data on a 1 m cell size grid covering the entire field of the HHLO. These datasets inform on local changes associated with slope failure, and seasonal topographical changes associated with clay shrinking and swelling.

	Sensors				
Location	**Moisture (sensor depth)**	**Matric potential (sensor depth)**	**Shape Accelerometer Array**	**Tiltmeters**	**Piezometers (borehole depth)**
1	0.2, 0.5 m	0.5 m	-	-	3.9 m
2	-	-	-	X	3.0 m
3	0.2, 0.5 m	0.5 m	-	-	-
4	0.2, 0.5 m	0.5 m	X	X	1.85 m
5	0.2, 0.5 m	0.5 m	X	X	2.35 m
6	0.2, 0.5 m	0.5 m	-	-	7.9 m

Table S1. Sensors available for this study per location (displayed on Figure 1)

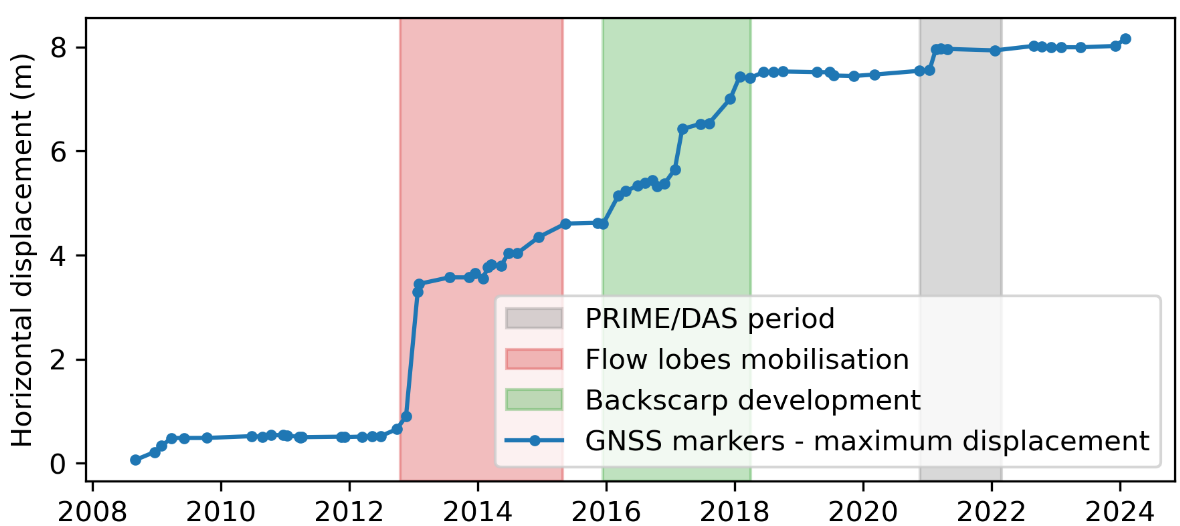

Figure S1. Maximum horizontal displacement recorded by GNSS survey on the set of GNSS markers. Since 2009, the landslide was most active between 2013 and 2018, with an average of 1.5 m/year maximum horizontal displacement recorded by the GNSS markers. Primary deformation occurred first on the flow lobes in 2013 and then propagated to the top of the slope with the development of the backscarp from 2016 onwards. No significant displacement occurred until reactivation, albeit with lower intensity, in January 2021.

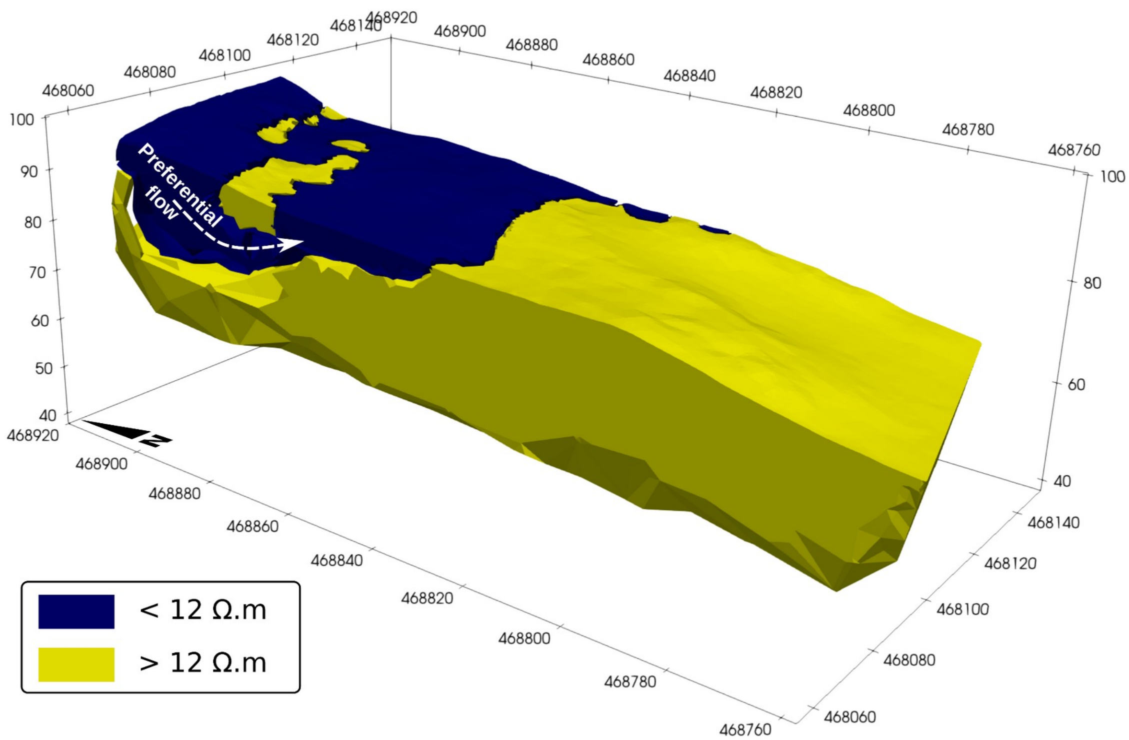

Figure S2. Model highlighting zones below and above 12 Ωm threshold on the 21 January 2021, highlighting most conductive zones which indicate potential preferential flow path underneath the backscarp.

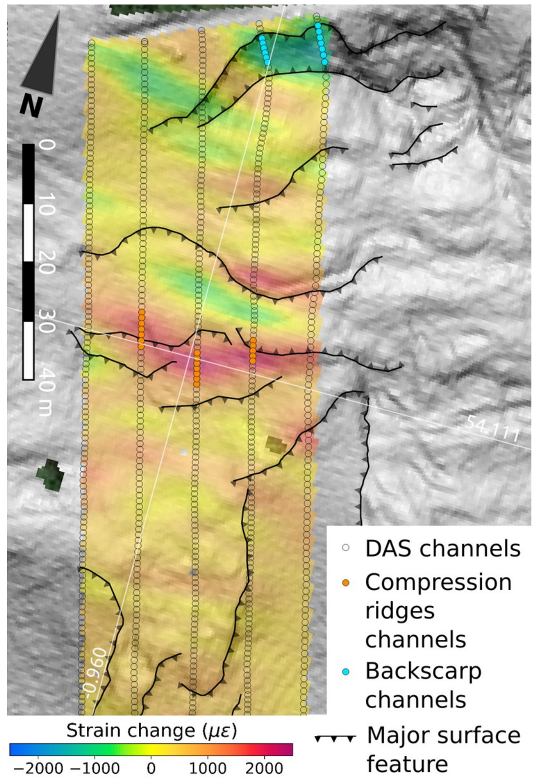

Figure S3. DAS channels used to determine the compression ridges and backscarp zones shown in Figure 3 of the main manuscript.

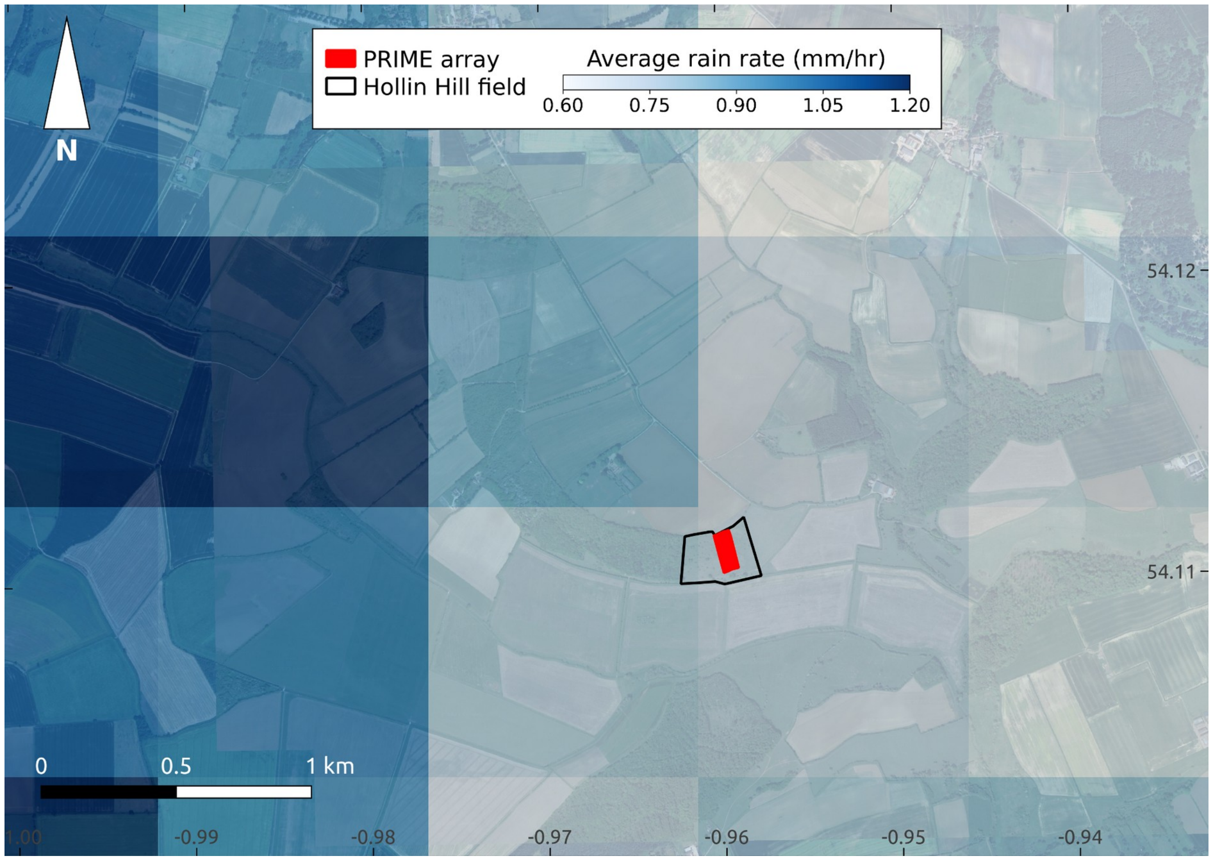

Figure S3: Average rain rate for the 30 minute window (22:00 to 22:30 UTC on the 20 January 2020) as collected by 1-km rainfall radar (5 minutes intervals) from the Met-Office Nimrod. This highlights the inhomogeneous rain rate in the area surrounding the HHLO, with higher rain intensity on the upslope plateau.